GACP 3rd YEAR PROGRESS REPORT

Proposal Title: Top-of-Atmosphere Clear-Sky Broadband Radiative Flux and Direct Aerosol Radiative Forcing from Satellite Measurements

Investigators: Norman G. Loeb (PI); Yongxiang Hu (Co-I); Bing Lin (Co-I)
PI Affiliation: Hampton University, Hampton, VA
PI Address: Mail Stop 420, NASA Langley Research Center, Hampton, VA 23681
Email: n.g.loeb@larc.nasa.gov

GOALS

The accuracy of satellite-derived estimates of top-of-atmosphere (TOA) aerosol radiative forcing (natural + anthropogenic)—also known as the direct radiative effect of aerosols—depends critically on the accuracy of shortwave (SW) and longwave (LW) TOA radiative fluxes. Since satellites cannot directly measure flux instantaneously, assumptions are needed to account for the angular and spectral dependence of the radiation field to convert a radiance measurement to a flux estimate. If these assumptions are incorrect, they will lead to errors in TOA radiative flux, and hence, aerosol radiative forcing.

In this investigation, measurements from the Clouds and the Earth's Radiant Energy System (CERES) instrument are used to determine the direct radiative effect of aerosols over ocean. A unique advantage of CERES is that the measurements are broadband, thereby eliminating the need for assumptions on the spectral dependence of the radiance field. However, models are needed to convert the broadband radiances to TOA radiative fluxes. The first part of this investigation involves the development of empirical angular distribution models (ADMs) for converting observed broadband radiances to fluxes over cloud-free oceans. Fluxes based on the new ADMs are then combined with imager retrievals of aerosol optical depth to determine the spatial and temporal dependence of the aerosol direct effect over the tropical oceans.

To determine aerosol radiative forcing from CERES, an approach similar to that outlined in Haywood et al. (1999) is used. The aerosol direct radiative effect is obtained from the difference between a no-aerosol flux inferred from the measurements and the diurnally averaged regional flux from CERES.

Summary of Accomplishments: Year 3

- Refined SW and LW ADM using more recent version of CERES cloud mask.
- Estimated "no-aerosol" TOA flux from CERES albedos and VIRS-based aerosol optical depths (based on Stowe et al., 1997 algorithm). Compared with theoretical estimate.
- Applied TOA fluxes with new ADMs and "no-aerosol" model to nine months of CERES/TRMM measurements.
- Examined temporal and spatial variability of aerosol direct effect in regions of biomass burning.
- Estimated uncertainty in direct radiative effect due to cloud contamination.
- Examined wind speed dependence of direct radiative effect and aerosol optical depth retrievals.
- Used CERES alongtrack measurements to estimate instantaneous albedo errors from CERES.

- Preparation and submission of 2 manuscripts for publication of GACP results.

Summary of Accomplishments from Previous Years

- Developed new approach for determining unfiltered CERES shortwave (SW), longwave (LW) and window (WN) radiances from *filtered* radiances measurements.
- Developed a new set of Anguar Distribution Models (ADMs) for estimating TOA fluxes from unfiltered CERES radiances.
- Performed theoretical broadband radiative transfer calculations to assist in ADM development and to compare estimates of the direct radiative effect with CERES.

Results

- The CERES instrument measures *filtered* broadband radiances in three channels: (i) shortwave (SW) between ≈ 0.2 to 5 μm; (ii) infrared window (WN) between ≈ 8 to 12 μm and (iii) total (TOT) between ≈ 0.2 to 200 μm. For scientific studies, SW, WN and longwave (LW) radiances that are independent of the instrument spectral response function characteristics are really what is needed. These *unfiltered* radiances are determined using a new procedure which significantly improves the accuracy of the unfiltered radiances, particularly for clear ocean scenes. The methodology, together with preliminary results, have been summarized in a paper published in *J. Applied Meteorology* (Loeb et al., 2000).
- TOA fluxes are estimated from the unfiltered radiances. This requires bidirectional reflectance models [or Angular Distribution Models (ADMs)] that account for the anisotropy in the measurements. For a given scene type "*j*", an ADM is defined as follows:

$$R_j(\theta_o,\theta,\phi) = \frac{\pi \bar{I}_j(\theta_o,\theta,\phi)}{\bar{F}_j(\theta_o)} \tag{1}$$

where $\bar{I}_j(\theta_o,\theta,\phi)$ is the 9-month mean radiance for a given interval of solar zenith angle θ_o, viewing zenith angle θ, and relative azimuth angle ϕ, and $\bar{F}_j(\theta_o)$ is the corresponding flux determined by integration of $\bar{I}_j(\theta_o,\theta,\phi)$ over all upwelling directions. 9 months of CERES/TRMM measurements were used to construct SW, LW and WN ADMs for clear ocean scenes. The SW ADMs were initially defined for 4 percentile intervals of wind speed. Figure 1 provideds an example of ADMs for θ_o = 30°-40°. The wind speeds are based on Special Sensor Microwave/Imager (SSM/I) retrievals that have been ingested into the ECMWF data assimilation analysis. Instantaneous fluxes are determined as follows:

$$\hat{F} = \frac{\pi I(\theta_o,\theta,\phi)}{R(w_k,\theta_o,\theta,\phi)\left(\frac{R^{th}(w_k,I)}{R^{th}(w_k,\bar{I})}\right)} \tag{2}$$

where $I(\theta_o,\theta,\phi)$ is the measured CERES radiance, w_k corresponds to the k^{th} wind speed interval, $R^{th}(w_k,I)$ and $R^{th}(w_k,\bar{I})$ are theoretically derived anisotropic factors inferred from $I(\theta_o,\theta,\phi)$ and the mean radiance $\bar{I}(w_k,\theta_o,\theta,\phi)$ that was used to derive

the ADM $R(w_k, \theta_o, \theta, \phi)$ for wind speed interval w_k. The ratio of theoretical anisotropic factors in Eq. (2) is introduced in order to account for the influence of aerosol optical depth on the anisotropy of the scene. Aerosols properties in the model calculations are based on the maritime tropical model of Hess et al. (1998). To ensure that this correction does not introduce a bias in the overall mean flux, fluxes estimated from Eq. (2) are normalized so that the mean estimated flux in each wind speed interval matches the flux $\overline{F}(w_k, \theta_o)$ determined by integrating $\overline{I}(w_k, \theta_o, \theta, \phi)$ over all upwelling directions.

- The accuracy of instantaneous CERES TOA SW fluxes are determined using CERES measurements from days when CERES was scanning in the alontrack direction. Figure 2 illustrates the procedure. Briefly, SW fluxes from multiangle CERES measurements located over 30-km targets along the ground track are collected. Next, instantaneous fluxes from all directions are converted to albedo and a dispersion parameter (*D*), defined as the standard deviation-to-mean SW albedo ratio, is determined for each 30-km target. Since the same region is observed from several angles, albedos from different directions should be the same. Figure 2 shows relative frequency distributions of the *D* based on fluxes estimated using the ADMs described above, fluxes from the CERES ERBE-Like product, and fluxes based on imager scene identification but assuming the targets are Lambertian (i.e. no anisotropic correction). As shown, fluxes based on Eqs. (1)-(2) show a factor of 4 improvement in consistentcy over the ERBE-Like product.

- The direct radiative effect of aerosols (or simply, "the direct effect") is inferred from the difference between the TOA flux from an atmosphere with and without aerosols as follows:

$$\Delta F(\lambda, \Phi, d) = \overline{F}_{na}(\lambda, \Phi, d) - \overline{F}_{a}(\lambda, \Phi, d) \qquad (3)$$

where $\overline{F}_{na}(\lambda, \Phi, d)$ is the daily average SW flux in the absence of aerosols for latitude λ, longitude Φ, and day d, and $\overline{F}_{a}(\lambda, \Phi, d)$ is the daily average SW flux in the presence of aerosols. Since aerosols are always present in the atmosphere, $\overline{F}_{na}(\lambda, \Phi, d)$ cannot be measured directly from satellite measurements. Instead, $\overline{F}_{na}(\lambda, \Phi, d)$ is inferred by a simple regression procedure. Instantaneous TOA fluxes from CERES are plotted against VIRS 0.63 μm aerosol optical depths in 1° solar zenith angle increments. VIRS 0.63 μm aerosol optical depths are retrieved using the 2nd generation NOAA/NESDIS algorithm (Stowe et al., 1997), which has been implemented in the CERES SSF production code. The intercept for these regressions—*i.e.* the TOA flux extrapolated to zero aerosol optical depth—approximates the "no aerosol flux" in each 1° solar zenith angle increment. Fig. 3 shows the albedo corresponding to $F_{na}(\theta_o)$ against solar zenith angle. Also shown is a 5th order polynomial fit (red line) to these points, and a DISORT (Stamnes et al., 2000) radiative transfer model calculation that accounts only for molecular scattering and absorption using k-distribution tables from Kato et al. (1999) (black line). The calculations assume a tropical atmosphere with ocean surface bidirectional reflectance based on a routine ("OCEABRDF") from the 6S

radiative transfer code (Vermote et al., 1997), which accounts for specular reflection (Cox and Munk, 1954), wind-speed dependent whitecaps (Koepke, 1984), and below water surface reflectance (Morel, 1988). Here a wind speed of 5 m s^{-1} is assumed. The model results in Fig. 3 are within 3% of $F_{na}(\theta_o)$ at solar zenith angles between 10° and 60°, and 5% elsewhere. This excellent agreement between theory and observation suggests that the model surface optics is well characterized in the calculations. $\overline{F}_{na}(\lambda, \Phi, d)$ for a given region is determined by averaging fluxes evaluated using the polynomial fit in Fig. 3 at all times of the day.

- Fig. 4 (a) shows the direct radiative effect of aerosols for all nine months of CERES/TRMM observations. The mean VIRS 0.63 μm aerosol optical depth for the same period is shown in Fig. 4 (b). Areas of maximum aerosol direct radiative effect are clearly evident near Central America due to biomass burning, and west of the Sahara desert associated with wind-blown dust. In these regions, the 9-month mean aerosol direct can be greater than -20 W m^{-2} with VIRS 0.63 μm aerosol optical depths as high as 1.0. Minima in the 9-month mean aerosol direct radiative effect appear along the equatorial Pacific and Indian Oceans where easterly trade winds are < 5 m s^{-1} (not shown). The direct radiative effect in these regions is typically -2 W m^{-2} and VIRS 0.63 μm aerosol optical depths range from 0.05-0.1.

- Latitudinal distributions of the direct radiative effect of aerosols and VIRS 0.63 μm aerosol optical depth are shown in Fig. 5. In both cases, a marked contrast between the northern and southern tropical oceans is evident. The direct radiative effect in the south is –3.6 W m^{-2} compared to -5.5 W m^{-2} in the north. The corresponding VIRS 0.63 μm aerosol optical depths are 0.11 and 0.17, respectively. Over all the tropics, the average direct radiative effect is –4.6 W m^{-2} and the average VIRS 0.63 μm aerosol optical depth is 0.14.

- Fig. 6 shows the relationship between the daily mean CERES direct radiative effect of aerosols and VIRS 0.63 μm average aerosol optical depth for 1° regions over the Pacific Ocean between 10° S - 20° N and 180° W - 90° W. The two are highly correlated (correlation coefficient 0.96) and clearly show the influence of aerosols on TOA radiation, with values as high as –80 W m^{-2} (VIRS 0.63 μm aerosol optical depth 2.5). As the aerosol optical depth approaches zero, the direct effect should also approach zero—in Fig. 4 it reaches 0.06 W m^{-2}, which is ≈ 1.3% (relative) of the tropical average aerosol direct radiative effect. The slope of the linear fit through the points—or the radiative effect of tropical aerosols per unit optical depth—is -32.1 W m^{-2} τ^{-1}.

- To examine the influence of biomass burning aerosols on TOA radiation during a dramatic fire event, we consider the 1998 Central American fires that occurred during a period of prolonged drought over Central America and southern Mexico (Peppler et al., 2000). Fig. 7 shows the spatial and temporal variation of the aerosol direct radiative effect and the corresponding VIRS 0.63 μm aerosol optical depth for three longitude intervals off of the coast of Mexico. The region furthest from the source of the biomass burning, between 140° W-120° W, has a minimum direct radiative effect of –2.4 W m^{-2} (aerosol optical depth of 0.08) in January, and a

maximum in June of –5 W m^{-2} (aerosol optical depth of 0.14). Between 120° W-100° W, the radiative effect ranges from –2.5 W m^{-2} (aerosol optical depth of 0.09) in January to –18 W m^{-2} (aerosol optical depth of 0.58) in May. Closest to the source region, between 100° W-90° W, a minimum of –4.7 W m^{-2} (aerosol optical depth of 0.17) occurs in January—likely due to urban pollution in Mexico City—to a maximum of –32.5 W m^{-2} (aerosol optical depth 0.96) in May due to biomass burning. These results are consistent with Christopher et al. (2000) who found instantaneous SW forcing over the same region and period of ≈ 68 W m^{-2}, which correspond roughly to a daily mean of 34 W m^{-2}.

- When the direct radiative effect of aerosols is stratified by wind speed, a small yet systematic trend is observed. Fig. 8 shows the direct radiative effect against wind speed for regions with mean VIRS 0.63 μm aerosol optical depths < 0.25 for 15° N - 25° N and 90° W to 180° W. As shown, the direct radiative effect becomes more pronounced over this region as wind speeds become stronger. This trend may be physical, as one might expect more sea-salt aerosol generation with increasing wind speed (Blanchard and Woodcock, 1980; Hoppel et al., 1990; Flamant et al., 1998), or it could be due to increased transport of aerosols from source regions. Alternately, this trend may instead be an artifact of the retrieval. For example, at large wind speeds, whitecap coverage may increase the observed reflectance from the surface, which can be misinterpreted as an increase in the aerosol direct effect. Haywood et al. (1999) found a similar trend in their comparison of the direct radiative effect of aerosols based on ERBE measurements. In that case, regions where the direct radiative effect was a maximum coincided with regions where the wind speed was a maximum. To unscramble the various factors that may explain this relationship, it may prove useful to examine statistics of remote marine aerosol optical depth with wind speed from the surface. In that case, the whitecap effect should be eliminated, but other factors, such as wind blown dust at the site and other meteorological influences, may obscure the results.

- One of the largest uncertainties in estimating the direct radiative effect of aerosols from satellite measurements is cloud contamination. The cloud mask involves several threshold tests to identify cloud-free CERES footprints. In the present study, footprints are assumed to be cloud-free if all VIRS pixels within a CERES footprint pass the reflectance, brightness temperature, and infrared/near infrared difference tests, and more than 50% pass the spatial homogeneity and 3.78 μm channel reflectance tests. The direct effect was also determined using thresholds of 0% and 100% for the percentage of VIRS pixels within a CERES footprint that must pass the spatial homogeneity and 3.78 μm channel reflectance tests. The 0% threshold includes all footprints that pass the reflectance, brightness temperature, and infrared/near infrared difference tests, while the 100% threshold requires all pixels within a footprint to also pass the spatial homogeneity and 3.78 μm channel reflectance tests. Fig. 9 compares the latitudinal dependence in the direct effect for a 50% threshold (solid circles) with results based on thresholds of 0% (bottom gray line) and 100% (top gray line). On average, the difference between the two extreme cases (i.e. 0% and 100%) is ≈ 0.8 W m^{-2}. The direct effect based on the 50% threshold is closer to the 100% threshold result (≈ 0.29 W m^{-2}) than it is to the 0%

threshold values (≈ 0.46 W m^{-2}). Unfortunately, it remains unclear how this error would change with higher-resolution imager measurements (e.g. 0.25 km MODIS measurements). The higher-resolution data would likely significantly improve detection of small-scale and thin clouds, which would tend to reduce the magnitude of the direct effect. However, there may also be conditions in which the current cloud mask is too restrictive and misidentify thicker aerosol layers for cloud. Clearly, more study is needed using instruments that are more sensitive to the presence of cloud (e.g. MODIS, PICASSO-CENA).

- For comparison, Fig. 9 also shows how the direct effect changes when the imager scene identification is replaced by scene identification from the CERES/TRMM "ERBE-Like" product (open circles), and when both the ERBE-like ADMs and scene identification are used to determine the direct effect (solid triangles). The ERBE-like product uses the Maximum Likelihood Estimation Technique (MLE) (Wielicki and Green, 1989) applied to CERES broadband radiances in order to classify a footprint as either clear, partly cloudy, mostly cloud or overcast. ERBE ADMs were derived from Nimbus-7 Earth Radiation Budget (ERB) measurements (Suttles et al., 1988). When ERBE-like clear ocean scene identification is used in conjunction with ADMs constructed from the SSF (open circles), the direct effect changes by ≈ -4 W m^{-2} (or a factor of 2) over what is obtained when the imager is used for scene identification. The difference is slightly smaller (≈ -3 W m-2) when ERBE-like ADMs are used with MLE scene identification (solid triangles). Clearly, this extra "forcing" is caused by cloud contamination. For ERBE, the cloud contamination problem is likely even more pronounced as the ERBE footprint is a approximately 4 times larger than that of CERES/TRMM.

References

Blanchard, D.C., and A.H. Woodcock, 1980: The production, concentration, and vertical distribution of the sea-salt aerosol. *Annals New York Acad. Sci.*, **338**, 330-347.

Cox, C., and W. Munk, Some problems in optical oceanography, *J. Mar. Res.*, **14**, 63-78, 1955.

Flamant, C., V. Trouillet, P. Chazette, and J. Pelon, 1998: Wind speed dependence of atmospheric boundary layer optical properties and ocean surface reflectance as observed by airborne backscatter lidar. *J. Geophys. Res.*, **103**, 25,137-25,158.

Haywood, J.M., Ramaswamy, V., Soden, B.J., 1999. Tropospheric aerosol climate forcing in clear-sky satellite observations over the oceans. *Science*, **283**, 1299-1303.

Hess, M., P. Koepke, and I. Schult, 1998: Optical properties of aerosols and clouds: The software package OPAC, *Bull. Amer. Meteor. Soc.*, **79**, 831-844.

Hoppel, W.A., J.W. Fitzgerald, G.M. Frick, R.E. Larson, and E.J. Mack, 1990: Aerosol size and optical properties found in the marine boundary layer over the Atlantic Ocean. *J. Geophys. Res.*, **95**, 3659-3686.

Kato, S., T.P. Ackerman, J.H. Mather, and E.E. Clothiaux, 1999: The *k*-distribution method and correlated-*k* approximation for a shortwave radiative transfer model, *J. Quant. Spectrosc. Radiat. Transfer*, **62**, 109-121.

Koepke, P., 1984: Effective reflectance of oceanic whitecaps. Appl. Optics, 23, 1816-1822.

Loeb, N.G., K.J. Priestley, D.P. Kratz, E.B. Geier, R.N. Green, B.A. Wielicki, P. O'R. Hinton, and S.K. Nolan, 2001: Determination of unfiltered radiances from the Clouds and the Earth's Radiant Energy System (CERES) instrument. *J. Appl. Meteor.*, **40**, 822-835.

Morel, A., 1988: In-water and remote measurements of ocean color. *Boundary-Layer Meteor.*, **18**, 177-201.

Nakajima, T., and M. Tanaka, 1986: Matrix formulations for the transfer of solar radiation in a plane-parallel scattering atmosphere. *J. Quant. Spectrosc. Radiat. Transfer*, **35**, 13-21.

Peppler, R.A., C.P. Bahrmann, J.C. Barnard, J.R. Campbell, M.-D. Cheng, R.A. Ferrare, R.N. Halthore, L.A. Heilman, D.L. Hlavka, N.S. Laulainen, C.-J. Lin, J.A. Ogren, M.R. Poellot, L.A. Remer, K. Sassen, J.D. Spinhirne, M.E. Splitt, and D.D. Turner, 2000: ARM Southern Great Plains site observations of the smoke pall associated with the 1998 Central American fires. *Bull. Amer. Meteor.*, **81**, 2563-2591.

Stowe, L.L., A.M. Ignatov, and R.R. Singh, 1997: Development, validation and potential enhancements to the second generation operational aerosol product at NOAA/NESDIS, *J. Geophys. Res.*, **102**, 16,923 – 16,934.

Vermote, E., D. Tanré, J.L. Deuzé, M. Herman, and J.J. Morcette, 1997: Second simulation of the satellite signal in the solar spectrum: An overview. *IEEE Transactions on Geoscience and Remote Sensing*, **35**, 675-686.

Wielicki, B.A., and R.N. Green, 1989: Cloud identification for ERBE radiation flux retrieval. *J. Appl. Meteor.*, **28**, 1133-1146.

GACP Bibliography:

Publications:

Loeb, N.G. and S. Kato, 2001: Top-of-atmosphere direct radiative effect of aerosols from the Clouds and the Earth's Radiant Energy System (CERES) satellite instrument. *J. Climate* (submitted).

Kato, K., and N.G. Loeb, 2001: Estimate of top-of-atmosphere albedo from a molecular atmosphere over ocean using the Clouds and the Earth's Radiant Energy System (CERES) satellite instrument, *J. Geophys. Res.* (submitted).

Oral Presentations:

Loeb, N.G., 2001: Aerosol Direct Radiative Effect From CERES. PICASSO-CENA Science Team Meeting, Hampton, VA, April 4, 2001.

Loeb, N.G., 2000: New perspectives on top-of-atmosphere aerosol signatures using CERES satellite data. Invited seminar at GFDL, Princeton, NJ, February 7, 2000.

Loeb, N.G., and Y. Hu, 1999: Top-of-atmosphere clear-sky broadband radiative flux and direct aerosol radiative forcing from satellite measurements. Presented at AGU Fall Meeting, December 13-17, 1999, San Francisco, California.

Loeb, N.G., 1999: Combining CERES, MODIS and PICASSO-CENA for Direct Aerosol Radiative Forcing Determination. PICASSO-CENA Science Team Meeting, Hampton, VA, November 2, 1999.

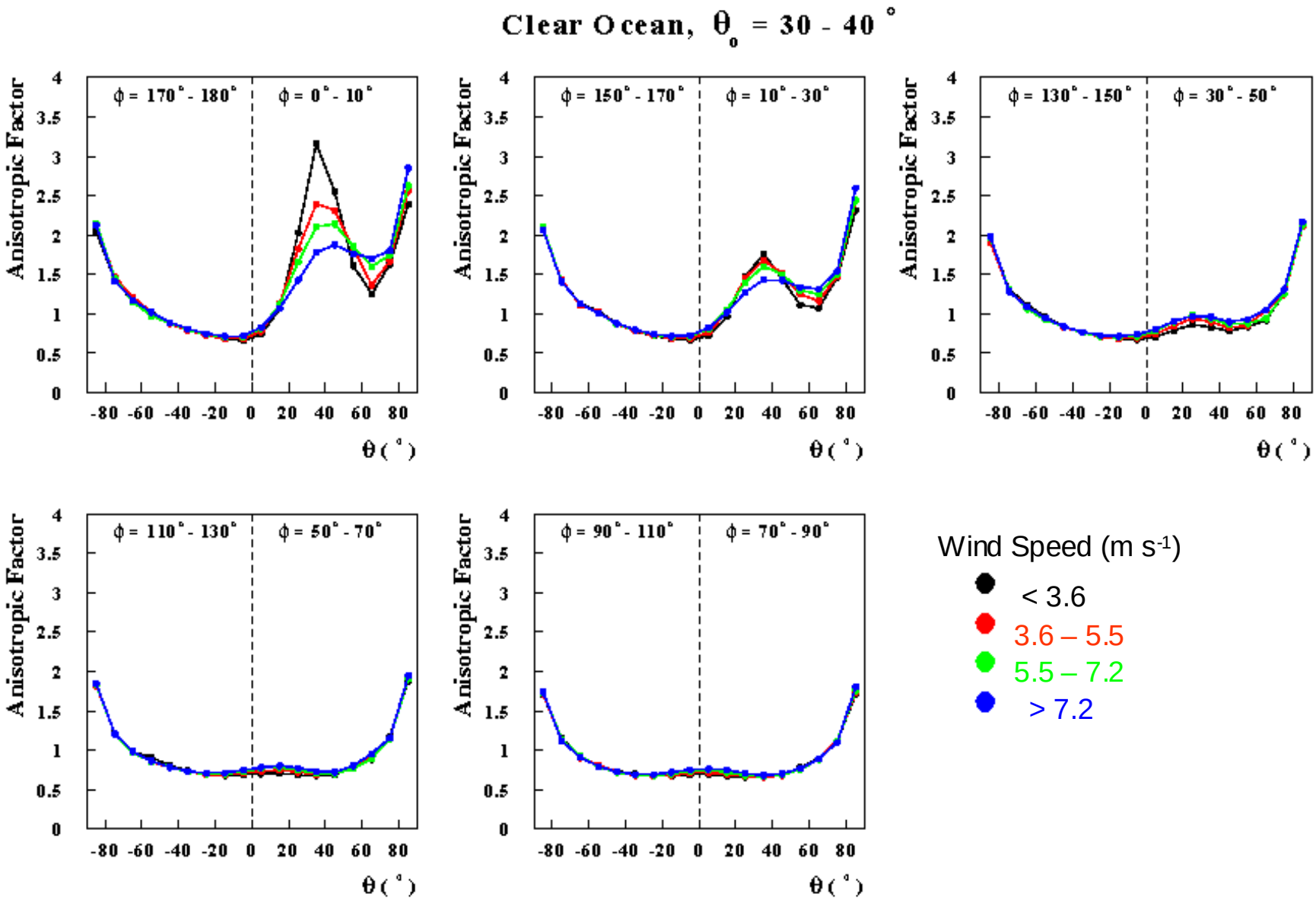

Figure 1 Clear ocean angular distribution models (ADMs) for solar zenith angles θ_o = 30°-40° as a function of wind speed.

TOA Flux Validation

Alongtrack Albedo Consistency Checks:

- Infer albedo from simultaneous measurements over 30-km regions at multiple angles.
- Compute albedo dispersion parameter:

$$D = \frac{\sigma_A}{\overline{A}} \times 100\%$$

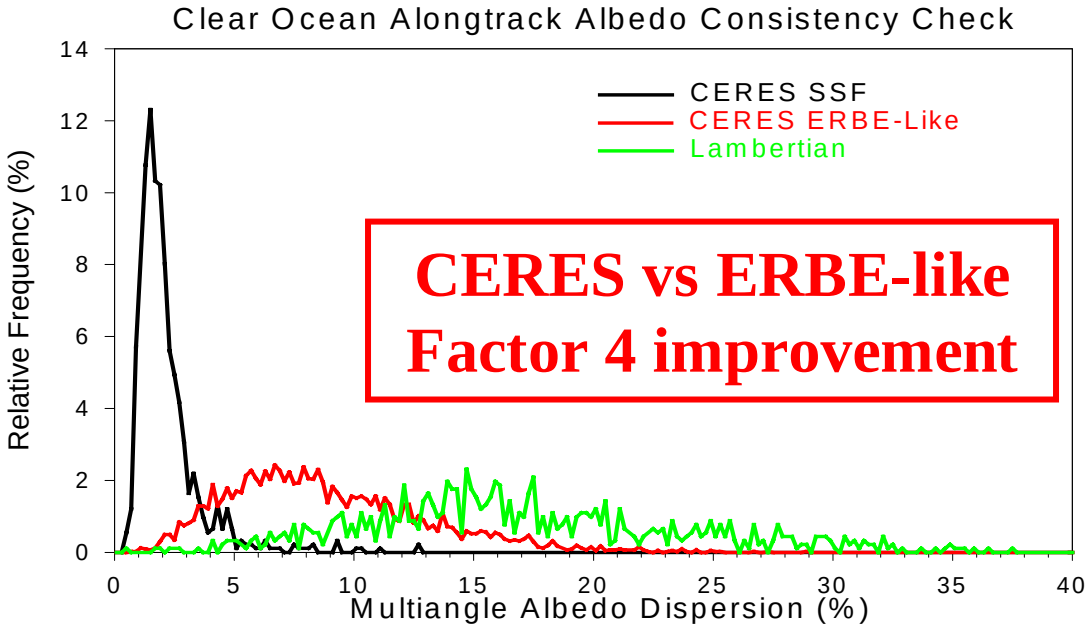

CERES vs ERBE-like
Factor 4 improvement

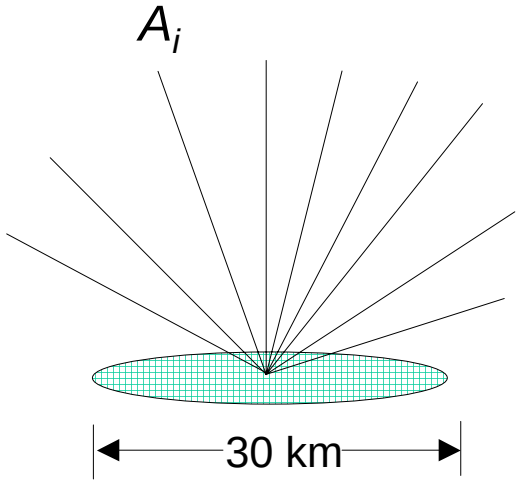

Average Dispersion (%)

CERES SSF = 2.2

CERES ERBE-Like = 8.8

Lambertian = 16.9

Figure 2 Illustration of how instantaneous albedo errors are determined using CERES alongtrack data.

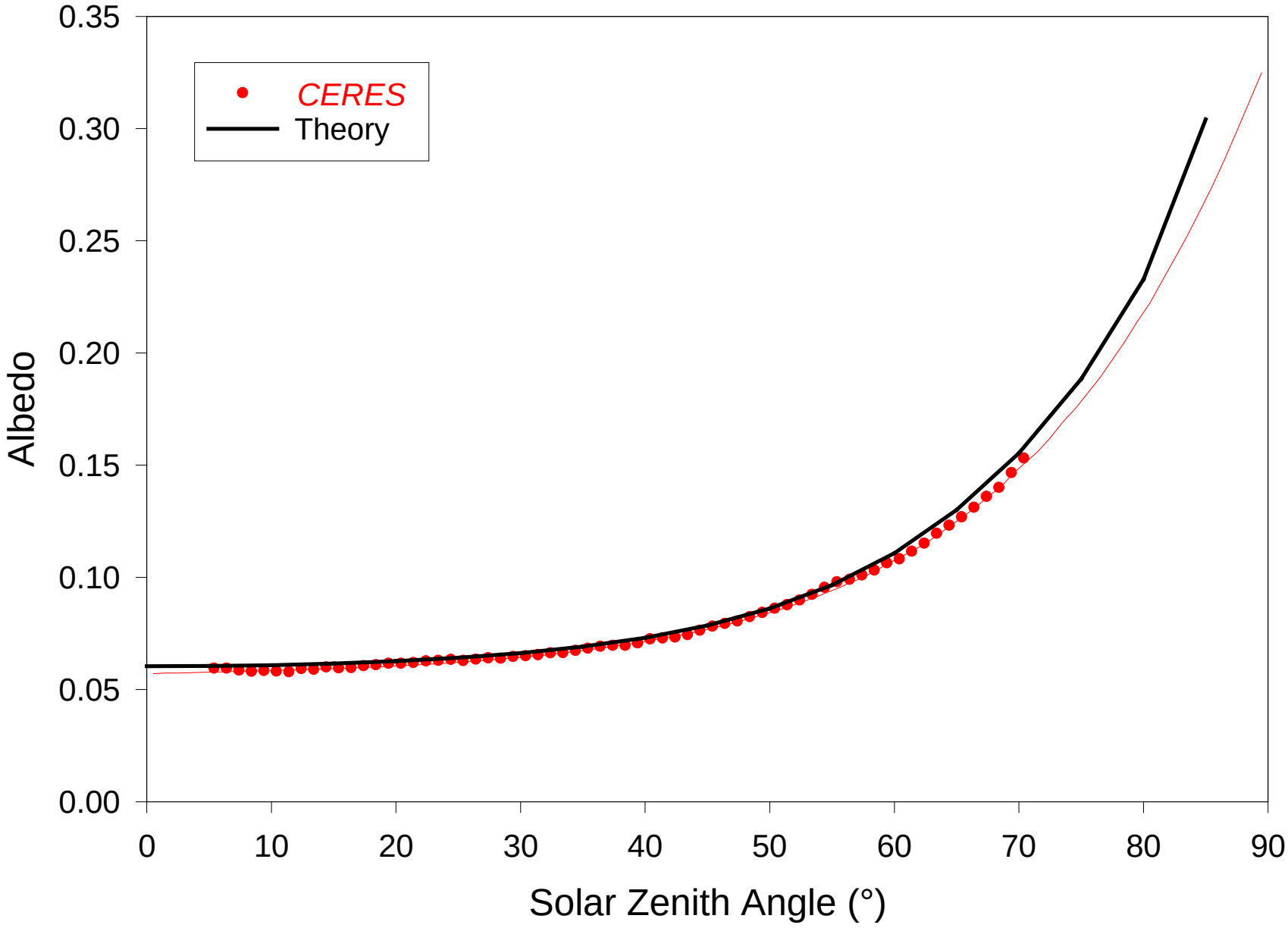

Figure 3 Albedo against solar zenith angle for the "no aerosol" atmospheric condition inferred from CERES (red circles) and theory (black line). Red line is a 5th order polynomial fit to the CERES result.

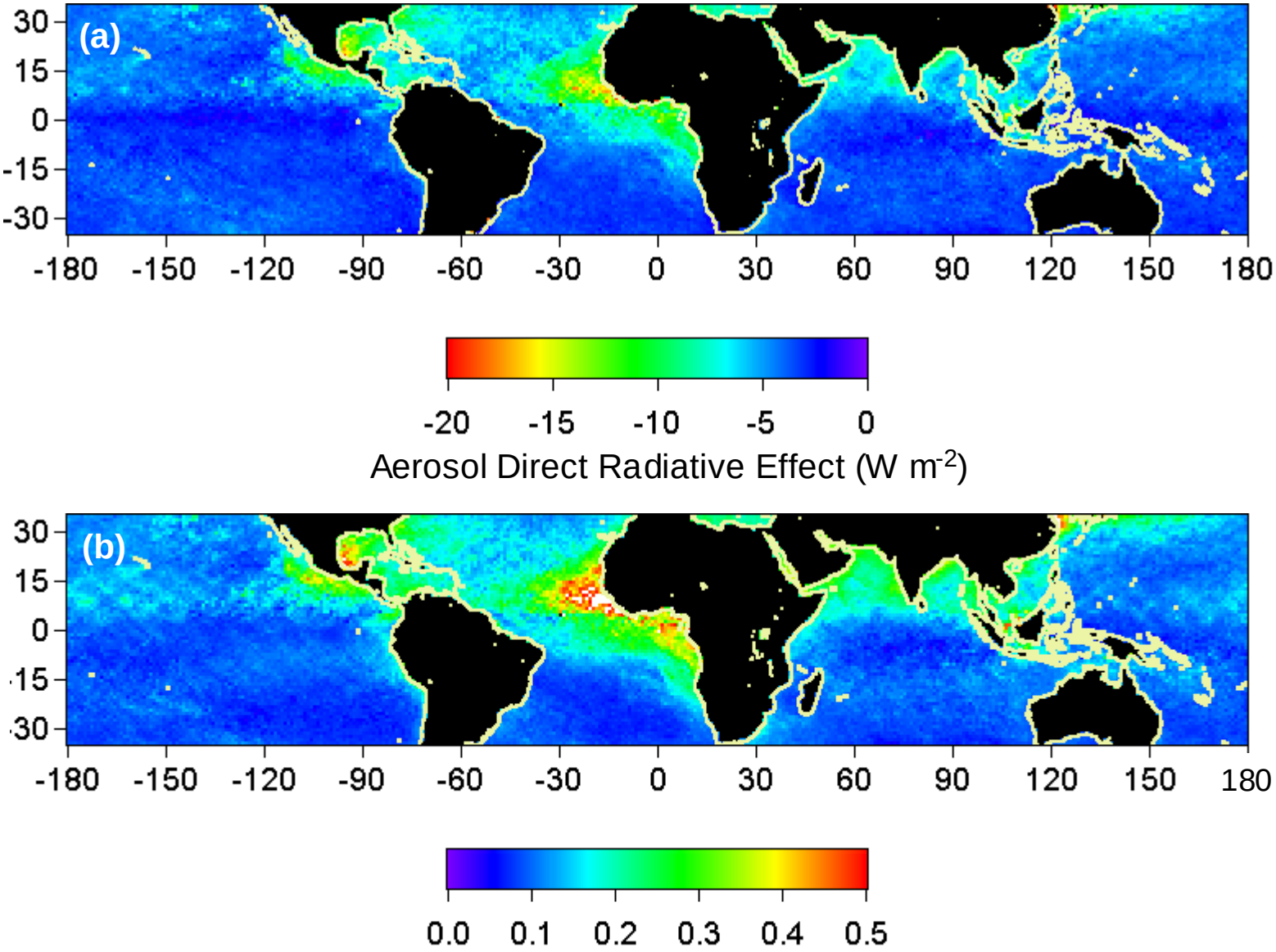

Figure 4 (a) Direct radiative effect of aerosols and (b) mean VIRS 0.63 μm aerosol optical depth from nine months of CERES and VIRS observations.

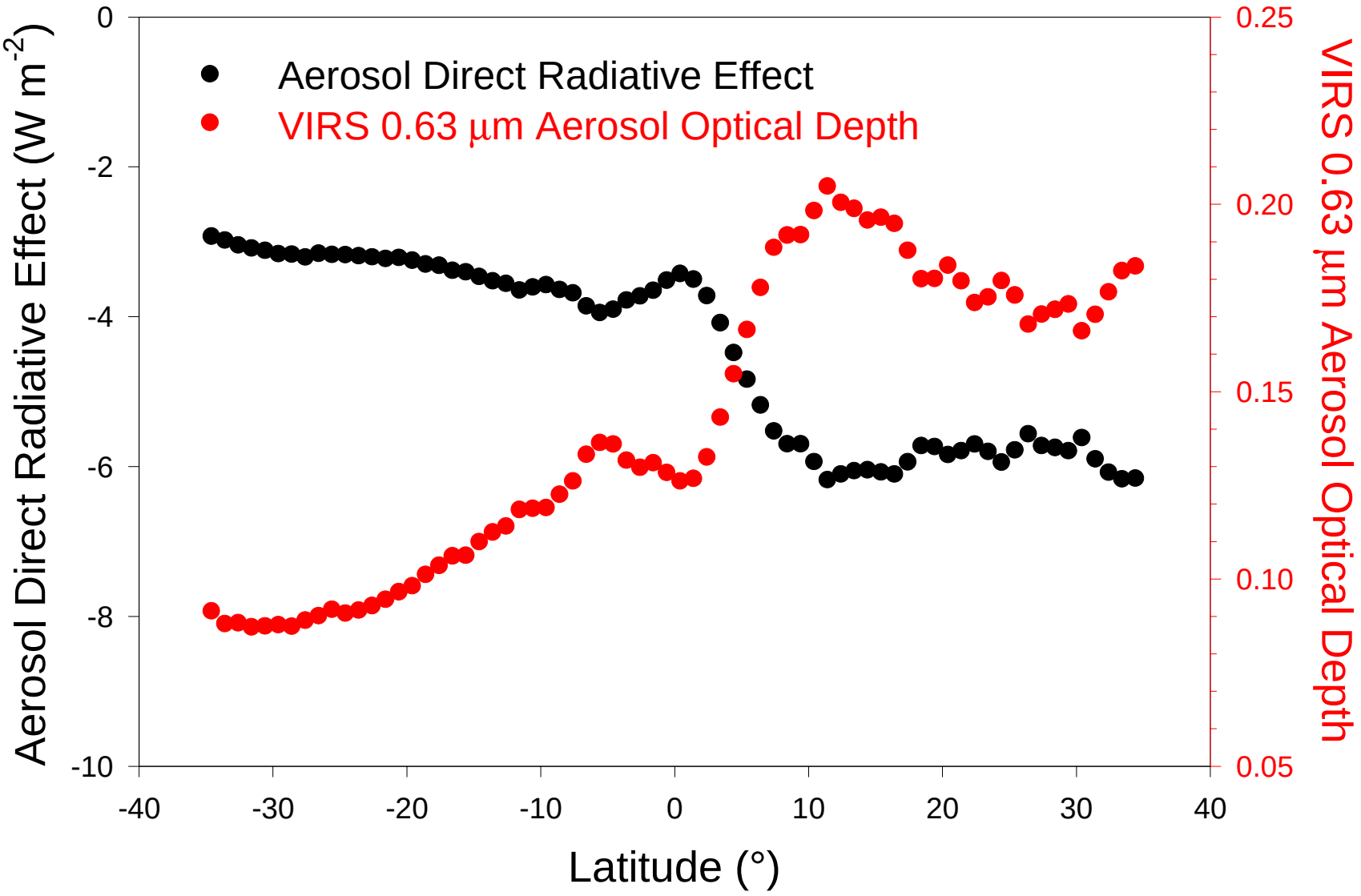

Figure 5 Latitudinal distribution of the direct radiative effect of aerosols and VIRS 0.63 μm aerosol optical depth.

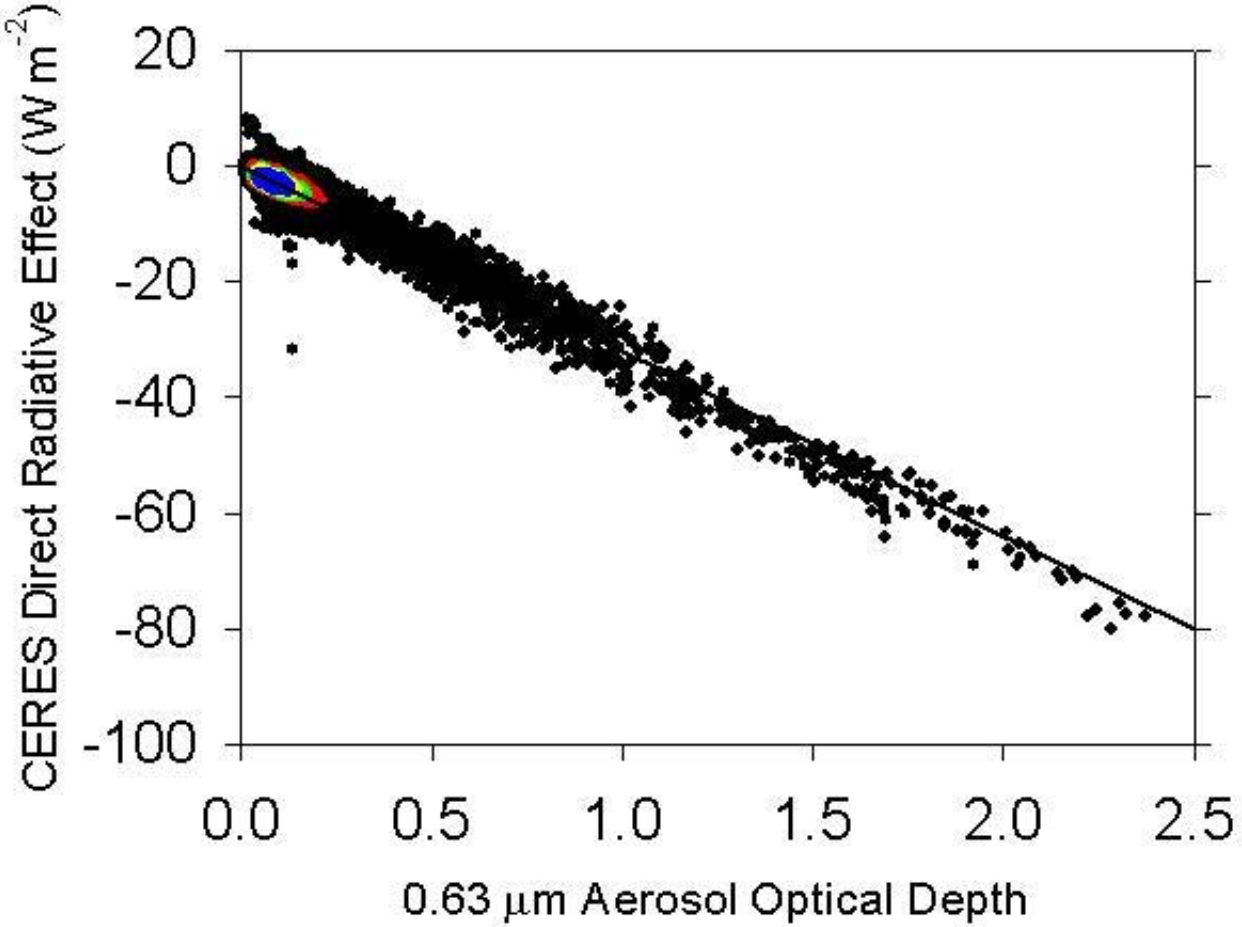

Figure 6 1° regional daily mean direct radiative effect of aerosols against VIRS 0.63 μm aerosol optical depth for 10°S - 20°N and 180°W - 90°W. Solid line is a linear regression fit through all data points.

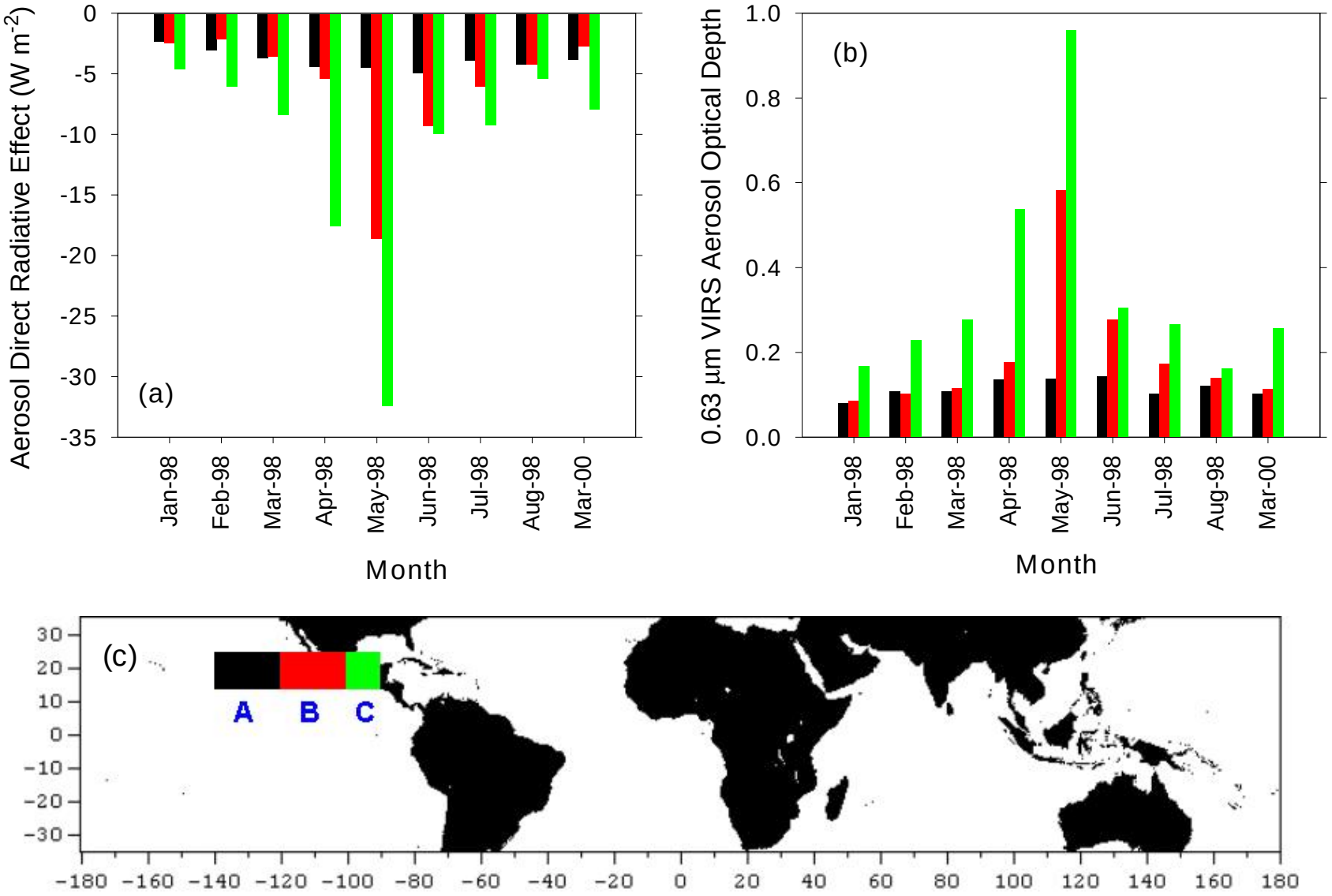

Figure 7 Spatial and temporal variation in (a) the direct radiative effect and (b) VIRS 0.63 µm aerosol optical depth for biomass burning aerosols over ocean near Mexico for the regions indicated in (c).

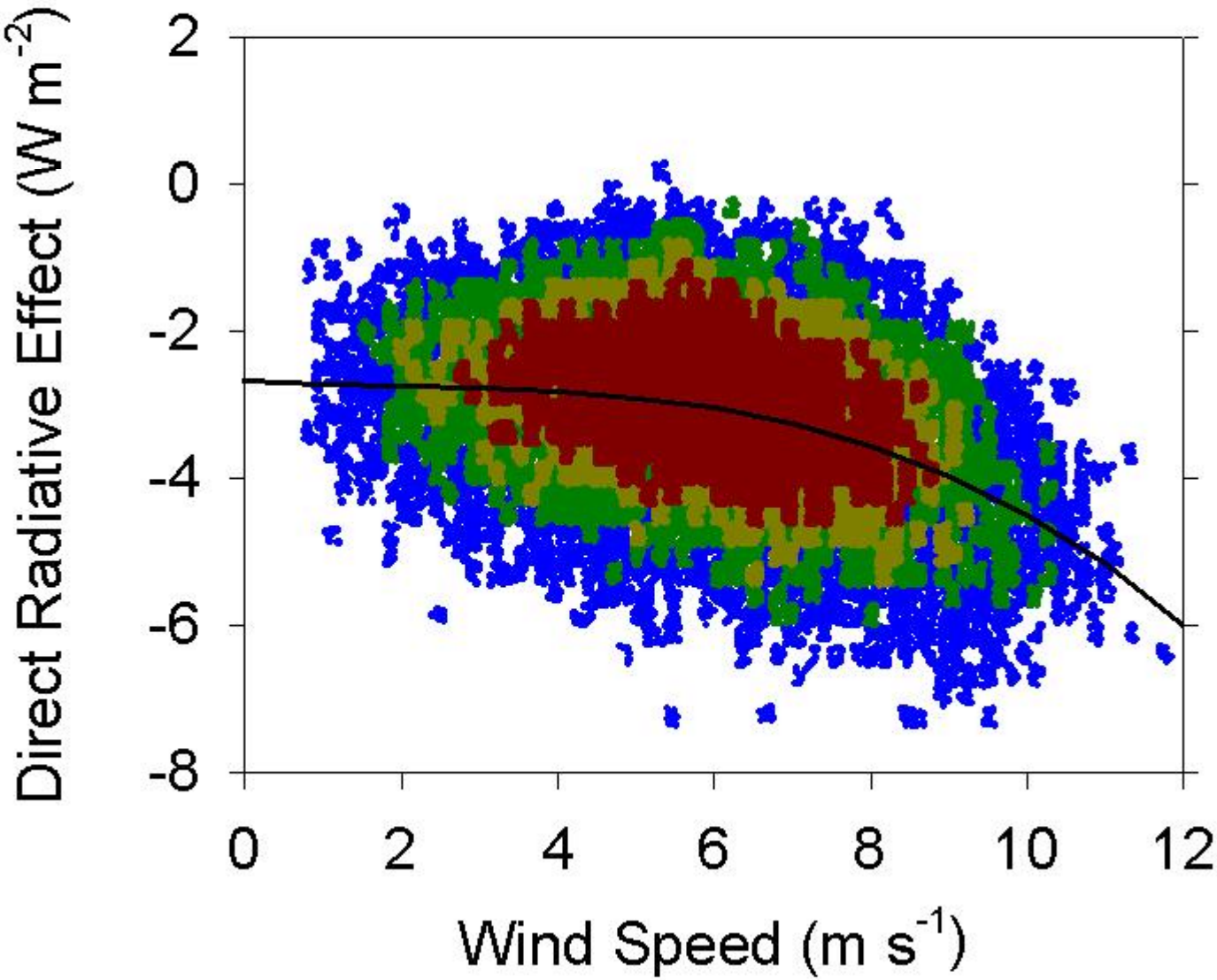

Figure 8 Aerosol direct radiative effect against wind speed for 1° regions with mean VIRS 0.63 μm aerosol optical depths < 0.25 for 15°N - 25°N and 90°W to 180°W. Solid line is a 3rd order polynomial fit through all data points.

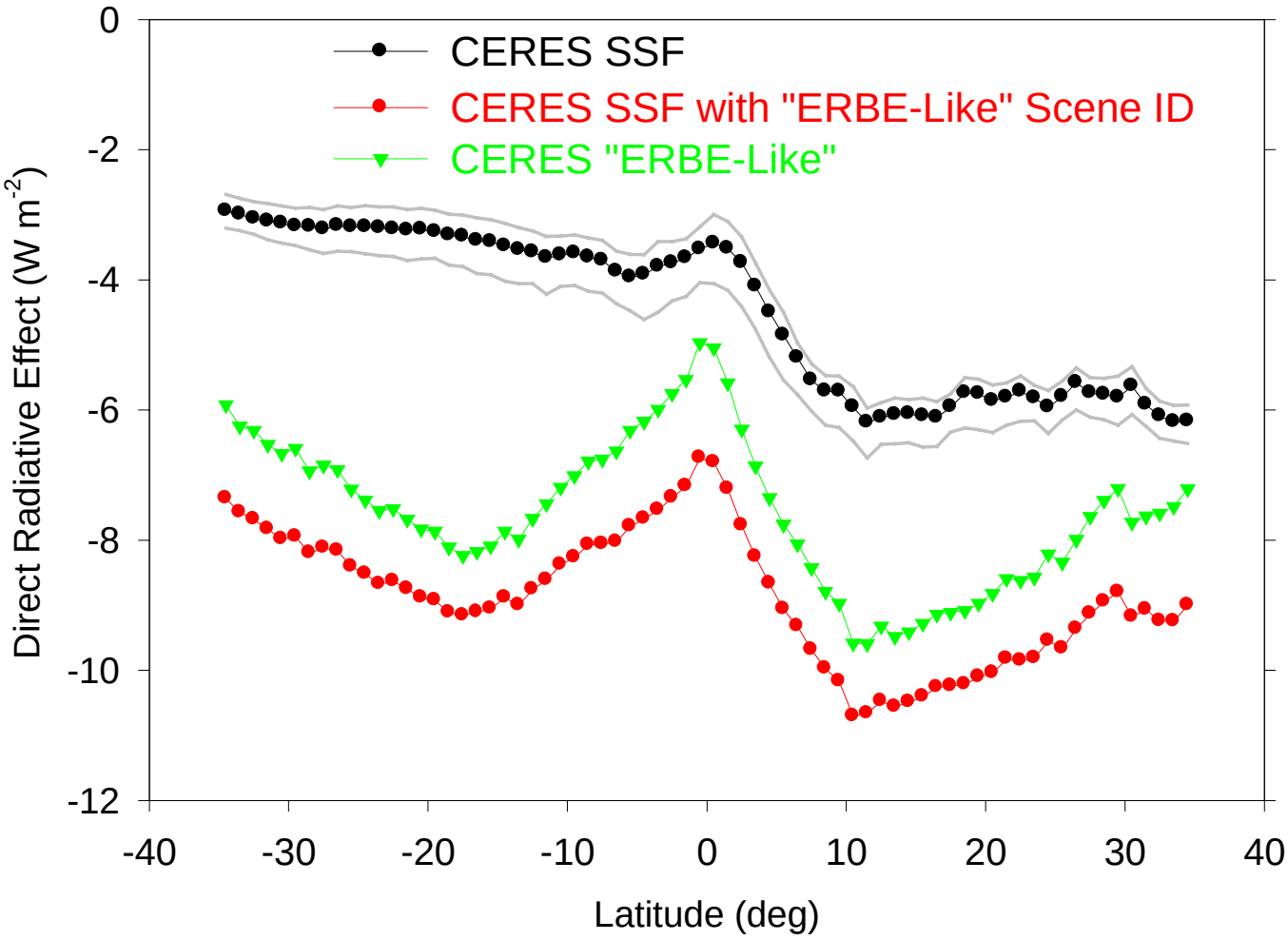

Figure 9 Sensitivity of aerosol direct radiative effect to clear-sky scene identification. "CERES SSF" result corresponds to CERES footprints with all VIRS pixels passing the reflectance, brightness temperature, and infrared/near infrared difference tests, and more than 50% passing the spatial homogeneity and 3.78 μm channel reflectance tests. Adjacent lines correspond to the case where the percentage of VIRS pixels passing the spatial homogeneity and 3.78 μm channel reflectance tests is 0% or more (lower gray line) and 100% (upper gray line). Red circles show the direct effect using SSF fluxes with scene identification from the CERES/TRMM "ERBE-Like" product. Green triangles show the direct effect when both TOA fluxes and scene identification are from the ERBE-Like product.